Supplementary Information for *Coupled electronic and magnetic excitations in the cuprates and their role in the superconducting transition*

Francisco Restrepo[1], Utpal Chatterjee[2], Genda Gu[3], Hao Xu[1], Dirk Morr[1,4], and Juan Carlos Campuzano[1]

[1] *Deptartment of Physics, University of Illinois at Chicago, Chicago, Illinois 60607, USA*
[2] *Department of Physics, University of Virginia, Charlottesville, Virginia 22904, USA*
[3] *Condensed Matter Physics and Materials Science Division, Brookhaven National Laboratory, Upton, New York 11973, USA*
[4] *James Franck Institute, University of Chicago, Chicago, Illinois 60637, USA*
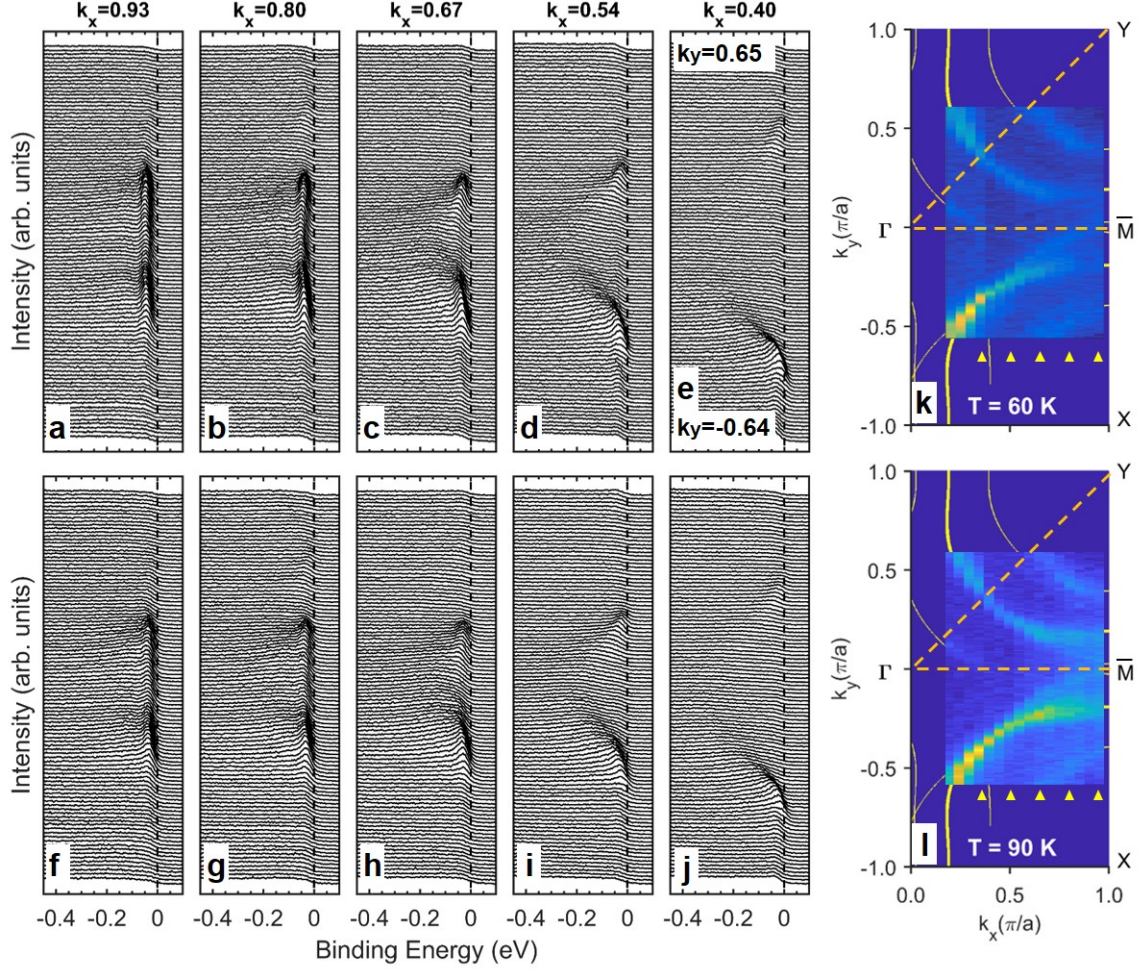
Supplementary Figure 1: **Selection of ARPES data from the Bi2212 single crystal below and near T_c.** **(a)** EDCs located at coordinates $\mathbf{k} = (0.93, -0.64 \rightarrow 0.65)\pi/a$ with $T = 60$ K (slice indicated by rightmost triangle in **(k)**). EDCs in **(b)** - **(e)** correspond to successively lower values of k_x (indicated by triangles in **(k)**). **(f)** - **(j)** show the same EDCs but at $T = 90$ K. **(k)** and **(l)** are the Fermi surface maps measured at $T = 60$ K and $T = 90$ K, respectively, laid over a tight binding fit to the dispersion [1].
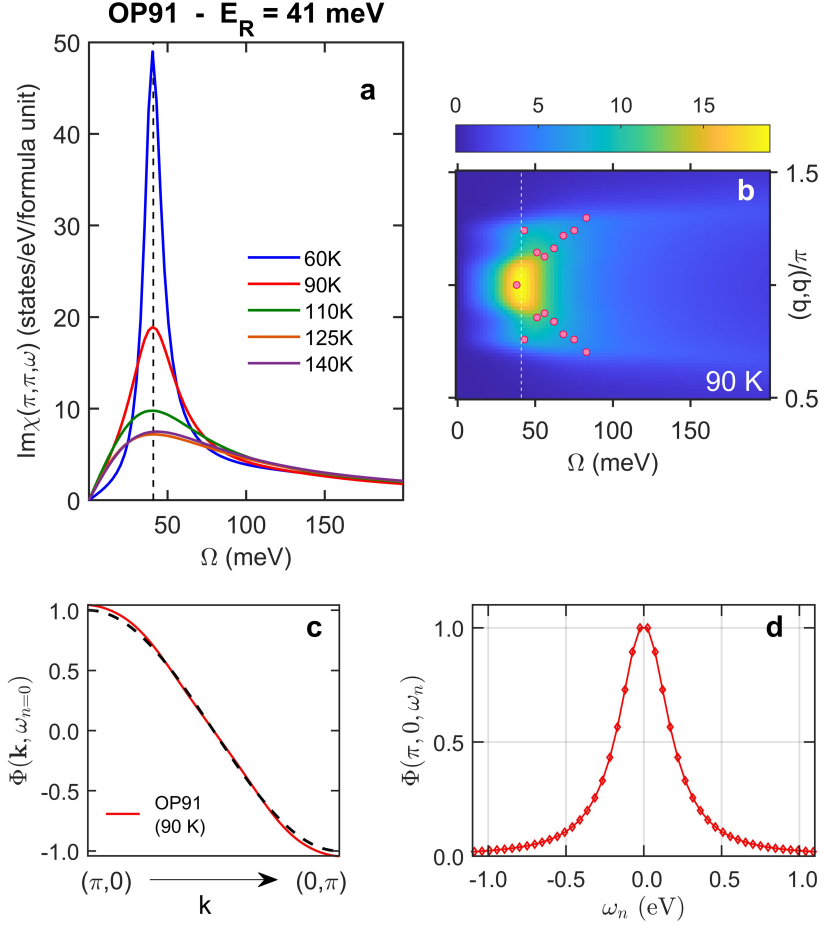
Supplementary Figure 2: **Additional calculations for the OP91 Bi2212 single crystal.** **(a)** ARPES-derived spin susceptibility at the commensurate wavevector (π, π) for temperatures between 60 K (below T_{c}) and 140 K ($\sim T^{*}$). **(b)** Energy-momentum dispersion of the spin susceptibility along the $(\pi/2, \pi/2) - (3\pi/2, 3\pi/2)$ direction. Pink symbols represent INS measurements (only above the resonance energy) from optimally doped Bi2212 at 100 K [2]. **(c)** Generalized order parameter for 90 K data along $(\pi, 0) - (0, \pi)$ direction (dashed line is the pure d-wave function $1/2(\cos k_x - \cos k_y)$). **(d)** Matsubara energy dependence of order parameter at $(\pi, 0)$ at 90 K.
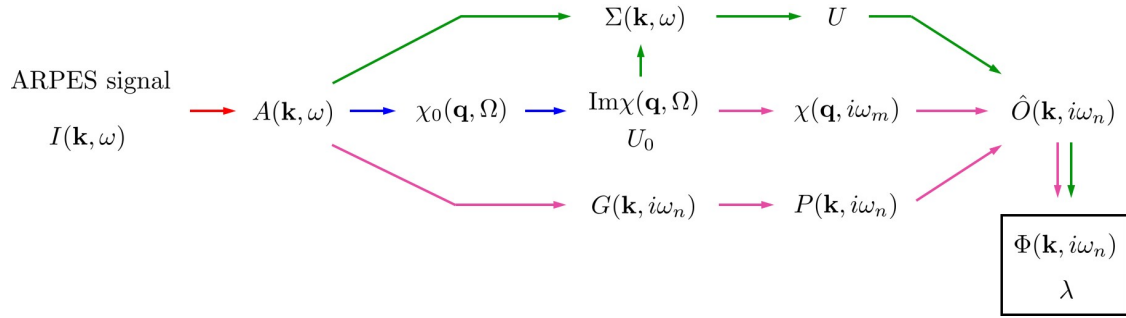
Supplementary Figure 3: **Roadmap of calculations presented in this work.** The red, blue, and pink steps are discussed in the main text, whereas the green steps are discussed in Supplementary Note 5.
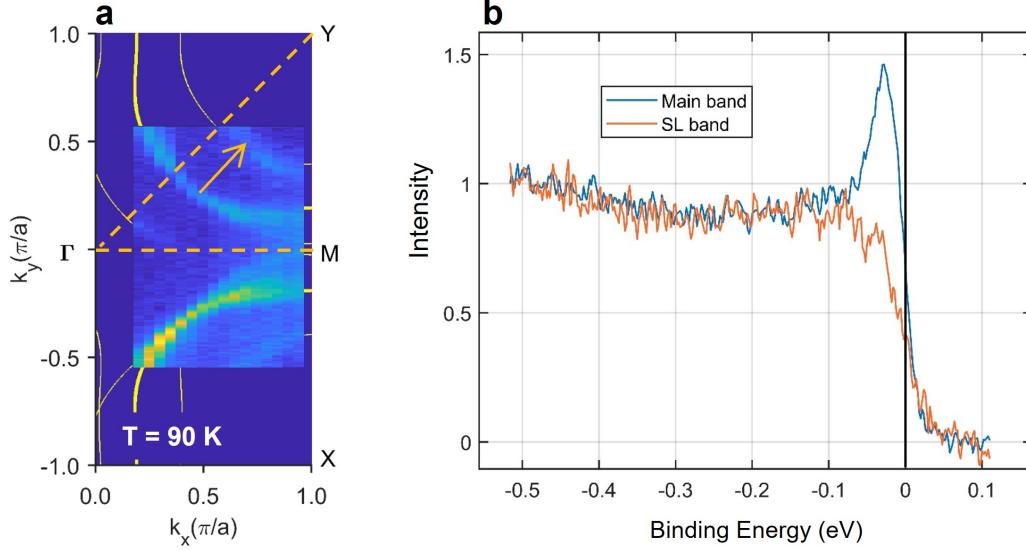
Supplementary Figure 4: **Comparison of ARPES spectra from the main and superlattice bands near the node.** **(a)** Raw Fermi surface map for Bi2212 for the OP90 sample at 90 K. **(b)** EDCs from the main (blue) and superlattice (orange) bands from points connected by the arrow in **(a)**.
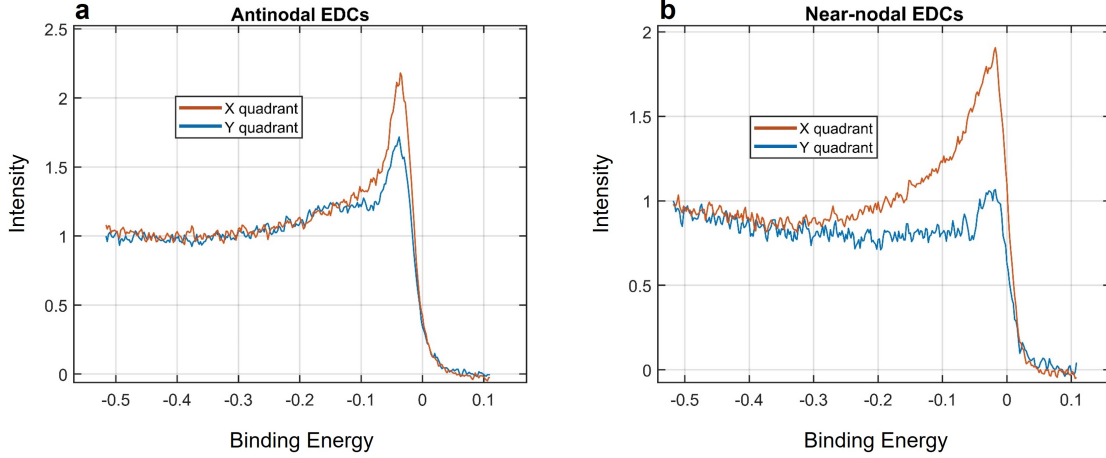
Supplementary Figure 5: **Comparison of ARPES near-nodal and antinodal spectra from the main band in the X and Y quadrants of the Brillouin zone. (a)** Energy Distribution Curves (EDCs) from the X (blue) and Y (orange) quadrants near the antinode. **(b)** EDCs from the X (blue) and Y (orange) quadrants near the node.
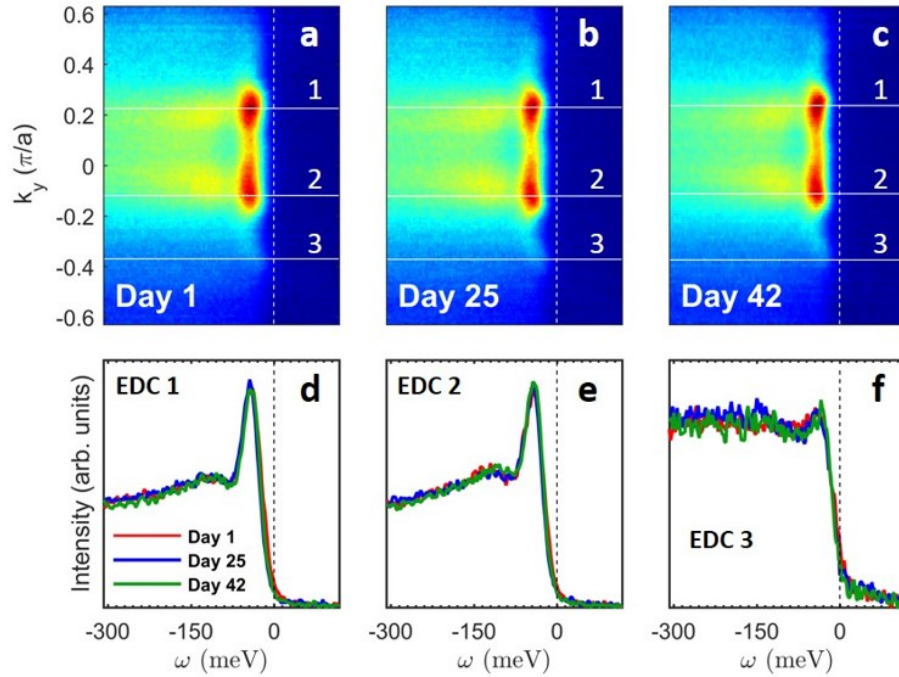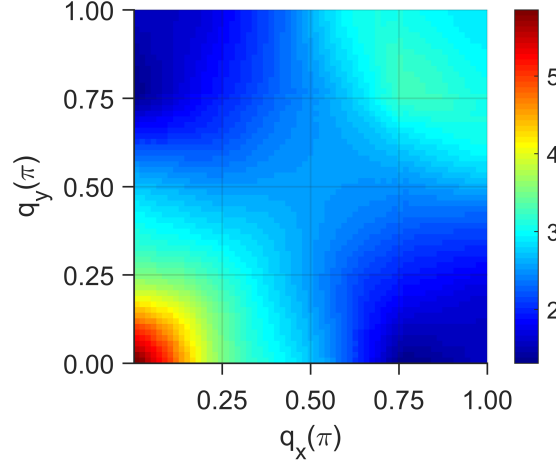

Supplementary Figure 6: **Absence of doping or contamination in the superconducting Bi2212 OP91 single crystal.** ARPES data in **(a)** - **(c)** were collected along the $(\pi, -\pi) \rightarrow (\pi, \pi)$ direction on days 1, 25, and 42 after cleaving. **(d)** - **(f)** show selected EDCs (labeled 1, 2, 3) indicated in **(a)** - **(c)**. All data were collected at 60 K, below T_c.

Supplementary Figure 7: **Real part of the bare susceptibility at $\omega = 0$ for an optimally doped Bi2212 sample at 140K (normal state).** The color bar is in units of states/eV/formula unit.
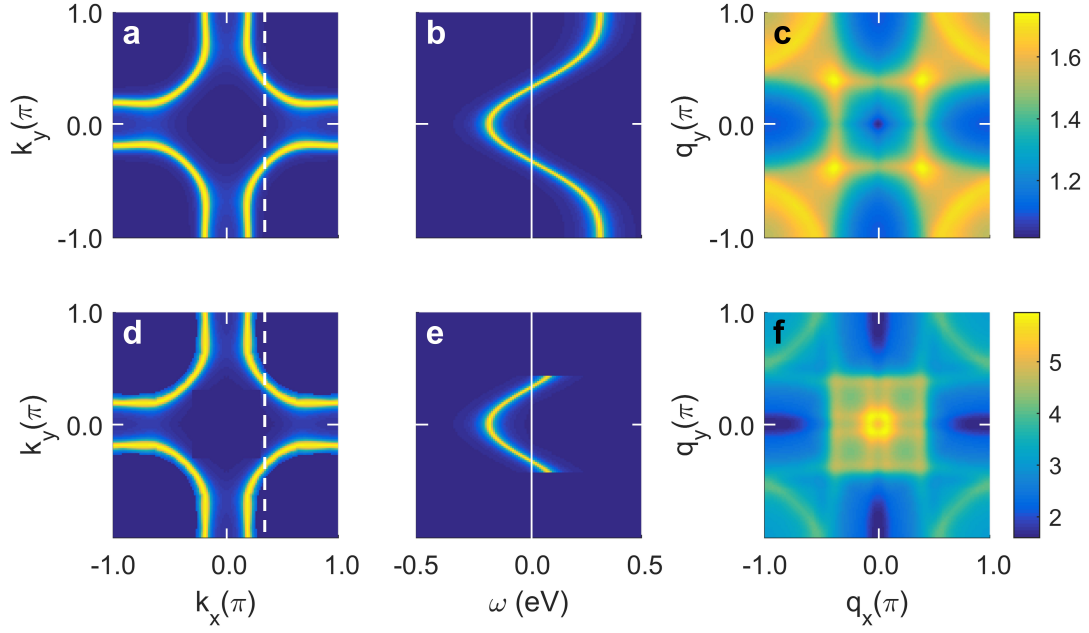
Supplementary Figure 8: **Effects of symmetrization on the bare susceptibility χ_0.** **(a)** Fermi surface of the true spectral function. **(b)** Dispersion along direction indicated by white vertical line in **(a)**. **(c)** Calculated $\chi_0(\mathbf{q}, \Omega = 0)$. **(d)**-**(f)** Same as **(a)**-**(c)** but the spectral function has been symmetrized "by hand" and some patches of the Brillouin zone have been removed. Color bars in **(c)** and **(f)** are in units of states/eV/formula unit.

.
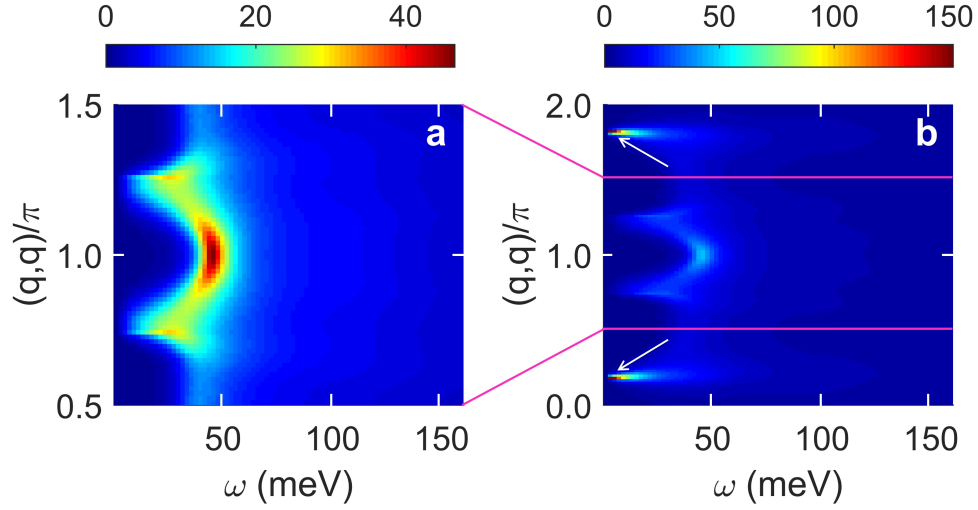
Supplementary Figure 9: **Symmetrization artifacts in the interacting spin susceptibility of near-optimally doped Bi2212.** **(a)** ARPES-derived magnetic excitation spectrum along diagonal direction from $(0.5\pi, 0.5\pi)$ to $(1.5\pi, 1.5\pi)$ **(b)**. Same as **(a)**, but in a momentum range $(0,0) - (2\pi, 2\pi)$. Note the difference in color bar scales (states/eV/formula unit).
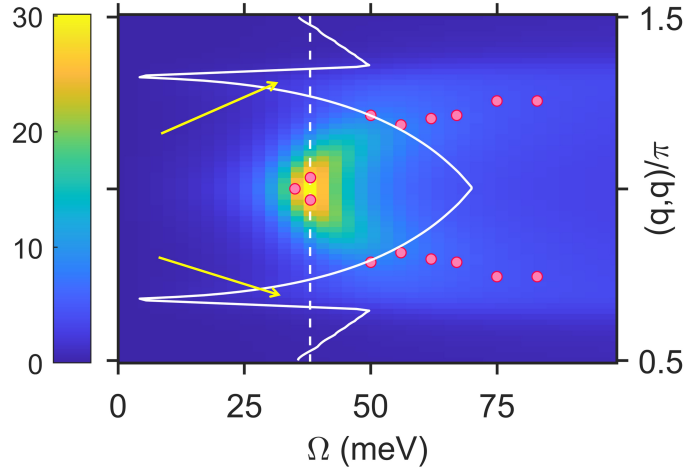
Supplementary Figure 10: **Spectrum of magnetic excitations for the OP80 film at 20 K.** The white curve is the lower boundary of the "particle-hole continuum". Pink symbols represent inelastic neutron scattering (INS) measurements only above the resonance energy from optimally doped Bi2212 at 10 K [2]. The color bar is in units of states/eV/formula unit.
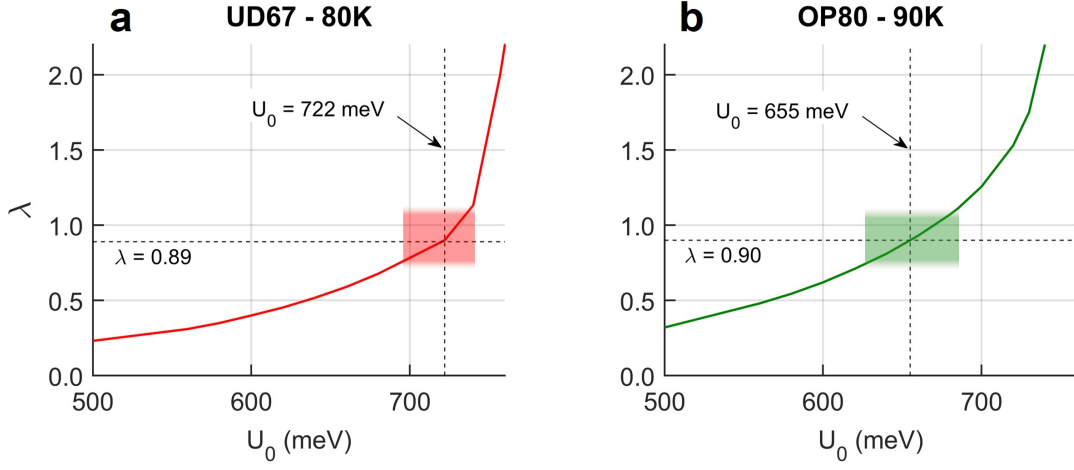
Supplementary Figure 11: **Dependence of the leading eigenvalue on the coupling energy U_0 above (but close to) T_c.** Results are shown for the thin films UD67 at 80 K in **(a)** and OP80 at 90 K in **(b)**. Shaded rectangles indicate uncertainties in U_0 and λ.

Supplementary Table 1: Comparison between the coupling energies (U_0 and U) and between the corresponding eigenvalues (λ_0 and λ respectively) near T_c

Sample	T (K)	U_0 (meV)	U (meV)	λ_0	λ
UD67	80	720	775	0.89	**1.02**
	62	741	820	0.87	**1.1**
OP80	90	655	635	0.9	**0.86**
	70	660	635	1.01	**0.93**
OP91	90	585	525	1.05	**0.84**

Supplementary Note 1. Additional data and results for the OP91 single crystal

In the main text we showed a small sample of the data sets employed in this work for the calculation of the pairing interaction and the solution of the Bethe-Salpeter Equation (BSE). Supplementary Figure 1 shows a more detailed example of the kind of data used in said calculations, collected from the OP91 single crystal at 60 K and 90 K. Panel (k) shows the momentum dependence of electronic excitations at the Fermi energy below T_c for half the Brillouin Zone (BZ). As in the UD67 sample data (shown in the main text), the main and superlattice bands are visible, but the latter are more intense due to the long-range superstructure typical of single crystals. The dashed triangle indicates the portion of momentum space selected for reflection about the symmetry axes of the zone to obtain the spectra throughout the BZ. Panels $(a) - (e)$ show stacked Energy Distribution Curves (EDCs) along selected vertical slices of momentum space, starting near the (π, k_y) line and ending in a slice containing the node (see yellow triangles in panel (k)). For both temperatures, the dispersion of the main band is evident from the EDCs, as is the closing of the superconducting gap near the node. Even though the EDCs are shown for binding energies up to 450 meV, in the calculations in the main text we used the entire EDCs, sampled up to 510 meV for the OP91 sample.

Using these data, we followed the same procedure as in the main text to calculate the spin susceptibility and solve the BSE. Supplementary Figure 2 summarizes the results for the OP91 crystal, emphasizing those obtained at 90 K ($\sim T_c$). In real frequencies, Imχ again broadens and loses intensity as the temperature is increased (Supplementary Figure 2a), while the upward dispersion branch is still visible in Supplementary Figure 2b. Pink symbols in this panel represent INS data from optimally doped Bi2212 at 100 K [2]. The pairing eigenfunction Φ also changes sign upon crossing the BZ diagonal and decays with a similar energy scale as in the thin films (~ 250 meV), as shown in Supplementary Figure 2c,d.

Supplementary Note 2. Further details on data analysis

Supplementary Figure 3 summarizes the steps required to solve the BSE starting from the spectral function measured in ARPES. While the procedure for the extraction of the spectral function from the data was already discussed in the main text and the Methods section therein, in this note we address a few additional details that were omitted for brevity.

Effect of the assumption of particle-hole symmetry

STM data on Bi2212 cuprate superconductors show signatures of particle-hole (p-h) asymmetry in the single-particle density of states (DOS) of optimally doped samples, which becomes more prominent in the lightly doped samples. We, however, argue that the assumption of of p-h symmetry (in a small energy interval around the chemical potential) in the current work has no significant bearing on the end results. To this end, we explored a different symmetrization procedure of the data as follows: $\text{Im}G(\mathbf{k}, -\omega) = \text{Im}G(\mathbf{k}, \omega)$. In other words, the spectral function was extended to all energies at all momenta. This approximation is certainly worse than that employed in this work. Even this procedure resulted in eigenvalues increasing with decreasing temperature and approaching unity for $T \sim T_{\text{c}}$, which is indicative of the lack of sensitivity of the end results of our analysis to the issue of p-h symmetry or its absence in ARPES data. Moreover, in our earlier work [3], we incorporated p-h asymmetry by hand in the calculation of the spin response function and found the results were not significantly different from the analysis invoking p-h symmetry. The lack of a significant impact of the issue of p-h symmetry in our analysis can be ascribed to the following fact: it is the *coherent* part of the electronic excitations which underlie the magnetic excitations. In this context, as shown in the past works of Randeria et al. [4] and Anderson et al. [5], the p-h asymmetry in single-particle DOS can predominantly be attributed to the p-h asymmetry of the *incoherent* electronic excitations—while the coherent part of the spectrum remains mostly p-h symmetric.

Superlattice contributions

In this work, the ARPES data from Bi2212 single crystals were collected in the Y-quadrant, which guarantees the absence of any intermixing between main bands (MBs) and superlattice bands (SLBs). In the thin films (UD67 and OP81 samples considered in this work), this does not constitute a significant issue because the SLB signal is much weaker compared to that in single crystals, due to lack of long-range superstructure order in thin films. Even though the SLB signal in single crystals is stronger than in thin films, the ratio of the intensity of SLB to that of the MB is weak in both cases. This is illustrated in Supplementary Figure 4, where, despite the fact that the SLB looks comparable to the MB in the Fermi surface map (panel (a)), the EDCs show that the main band has substantially more spectral weight (panel (b)). Consequently, the background subtraction effectively eliminates most of the SLBs during the extraction of the spectral function from the raw data.

One may, in principle, pursue the analysis presented in this work using data from the X quadrant instead. However, the MB intersects two SLBs in this quadrant near the node, which is why the main band appears to be more intense in this region (as in Supplementary Figure 1k,l). Looking at the EDCs from "equivalent" momenta in the X and Y quadrants, we see that they are qualitatively different (see Supplementary Figure 5). Unfortunately, this is not a matrix element effect —rather, it is due to the unavoidable mixing of two bands due to structural distortion. Therefore, a simple re-scaling cannot make EDCs from symmetry-equivalent momenta in these two quadrants coincide. In short, the excitations from the X quadrant should not be taken as a representative of the electronic structure of the CuO_2 planes.

Bilayer Splitting

We do not observe well-defined antibonding bands in our data from optimally doped and underdoped Bi2212 samples. In other words, the intensity of the signal from the antibonding MB is much weaker than that from the bonding MB. As is the case for the weak SLB signal, the weak antibonding MB intensity also gets effectively eliminated because of background subtraction. In this context, even though bilayer splitting may be present in optimally doped samples, it is prominent in strongly overdoped Bi2212 samples [6, 7], which were not considered in the current work. In passing, we would like recall the work of Dahm et al. [8]. They performed a similar calculation to ours, but starting with INS data from a different cuprate superconduc-

tor, $YBa_2Cu_3O_{6.6}$. Because bilayer splitting is more pronounced in this compound, the authors had to take this effect into account explicitly. Yet, their conclusions are similar to ours; namely, that the Bethe Salpeter eigenvalue is ~ 1 and, thus, that spin fluctuations are sufficiently strong to mediate high-T_c superconductivity.

Sample "aging"

After prolonged ARPES experiments, Bi2212 samples are known to "age" because of surface doping in ultra-high vacuum conditions. Therefore, we repeatedly measured antinodal spectra and compared them with those collected at the beginning of the experiment. These measurements showed no signs of surface contamination or doping. Supplementary Figure 6 shows the absence of aging in our OP91 crystal after 42 days of measurements. Both the dispersion (along the zone boundary) and selected EDCs are nearly identical for data collected on days 1, 25 and 42 after a single cleave.

Supplementary Note 3. The anomalous Green's function

In the superconducting state, the particle-hole bubble χ_0 should include a term quadratic in the anomalous Green's function, which we call FF. We ignored this term in this work for three reasons:

- As pointed out by Chatterjee et al. [3], in the superconducting state, the calculated dynamic susceptibilities vary only slightly when one includes the anomalous Green's function. Inclusion of the FF term will certainly influence the *bare* susceptibility, but an appropriate readjustment of the coupling constant U_0 will keep the resonance in the interacting susceptibility at the correct energy.

- While we considered several data sets below T_c to illustrate the performance of the RPA in constructing the spin fluctuation propagator, for the calculation of the Bethe-Salpeter eigenvalue we restricted our analysis to temperatures slightly below and above T_c, where the FF term is not important.

- Similar results for the eigenvalues were obtained from an independent method of obtaining the prefactor U^2 in the pairing interaction V, as shown in Supplementary Note 5.

However, it is instructive to examine the effect of this term on the RPA energies U_0 in the superconducting state. To this end, we first expressed the real part of the bare susceptibility as $\text{Re}(\chi_0) = \text{Re}(\chi_0^G) + \text{Re}(\chi_0^F)$ (where the second term is the anomalous contribution coming from the FF term) and defined the ratio $\alpha = \frac{\text{Re}(\chi_0^F)}{\text{Re}(\chi_0^G)}$ [3]. Since χ_0^F is unknown, so is α. However, in a d-wave superconductor, $\text{Re}(\chi_0^F)$ and $\text{Re}(\chi_0^G)$ add constructively at the commensurate wave-vector, so we expect this ratio to be positive at (π, π). From the pole condition for the resonance, $1 - U_0\text{Re}(\chi_0) = 0$, we see that an enhancement of the real part of the bare susceptibility reduces U_0. To estimate this reduction, we computed $\text{Re}(\chi_0^G)$ as in the main text (using ARPES data below T_c) and expressed the real part of the *total* bare susceptibility as

$$\text{Re}(\chi_0) = \text{Re}(\chi_0^G)(1 + \alpha_{\text{BCS}}), \tag{1}$$

where the ratio α was calculated using BCS normal and anomalous spectral functions [9] and a tight-binding fit for the Bi2212 dispersion [1]. We considered superconducting state spectral functions with a Lorentzian lineshape, sampled over a momentum grid of 128×128 points and energies ranging from -1.5 to 1.5 eV. We also allowed for a finite width (Γ) of the spectral function and studied the effect of varying this width. The convergence factor δ was set to 10 meV, and superconductivity was included through the d-wave gap

$$\Delta(\mathbf{k}) = \frac{\Delta_0}{2}(\cos k_x - \cos k_y), \tag{2}$$

with $\Delta_0 = 35$ meV. Since we were only interested in the effect on the coupling constant U_0, we compared results only at the commensurate wave-vector (π, π). For $\Gamma = 40$ meV, $\alpha = 0.05$, leading to a 5% decrease in U_0. For $\Gamma = 20$ meV, $\alpha = 0.10$, leading to a 10% decrease in U_0. Finally, for $\Gamma = 0$ meV, $\alpha = 0.2$, leading to a 20% decrease in U_0. The values of U_0 reported in the main text do not take this reduction ($\sim 10\%$ for the more physically relevant case) into account because the data employed were collected near T_c.

Supplementary Note 4. Obtaining the spin susceptibility from ARPES data

The choice of RPA coupling U_q

Supplementary Figure 7 shows the ARPES-derived *bare* susceptibility $\chi_0(\mathbf{q}, \Omega = 0)$ for an optimally doped Bi2212 sample in the normal state[1]. The results agree qualitatively with those in ref. [1]. There is a pronounced, square-like signal enclosing the $\mathbf{q} = 0$ point, as well as an incommensurate response around $\mathbf{Q} = (\pi, \pi)$. However, there is also significant response at $\mathbf{q} = 0$, which is not seen in model calculations (Figure 1 of ref. [1]). This response was found to be an artifact of the Fermi cutoff on the spectral function.

To demonstrate the fictitious origin of the $\mathbf{q} = 0$ peak, we calculated χ_0 using Lorentzian spectral functions with tight binding fits for the dispersion of Bi2212. The procedure was essentially the same as in Supplementary Note 3, but setting $\Delta_0 = 0$ (for the normal state) and $\Gamma = 20$ meV. Supplementary Figures 8a,b show the Fermi Surface and the dispersion for the true spectral function (without symmetrization). The main band disperses (along the dashed line in panel (a)) all the way to the BZ boundary. The bare susceptibility (at $\Omega = 0$) for this spectral function (Supplementary Figure 8c) closely resembles similar calculations presented in ref. [1]. Note the absence of spectral weight at $\mathbf{q} = (0, 0)$. The second row shows similar calculations but now the spectral function has been multiplied by the Fermi function and symmetrized, to simulate the analysis we did with experimental data. The dispersion does not cover the entire BZ because particle-hole symmetry is only assumed to hold for small binding energies (in this case, we took 80 meV about the Fermi energy). We see that the resulting bare susceptibility (panel (f)) has significant spectral weight at the zone center (note also the difference in color bar scales). The artifact is thus a direct consequence of not having access to the complete spectral function (including the unoccupied states), a shortcoming which can only partially be mitigated through symmetrization.

This artifact is also apparent in the *interacting* susceptibility, approximated via

---

[1]The results in this section were derived from ARPES data (from a near-optimally doped Bi2212 single crystal) presented in earlier publications, e.g. refs. [10, 11], not the data used in the main text. We use these data here only for illustration purposes.

RPA as [12]:

$$\chi(\mathbf{q}, \Omega) = \frac{\chi_0(\mathbf{q}, \Omega)}{1 - U_q \chi_0(\mathbf{q}, \Omega)}. \tag{3}$$

If U_q is momentum-independent, $\chi(\mathbf{q}, \Omega)$ possesses an anomalously strong peak near $\mathbf{q} = 0$, which is not seen in INS measurements. In Supplementary Figure 9 we compare the magnetic dispersion for $\mathrm{Im}\chi$ calculated with a momentum-independent coupling $U_q = U_0$ from $\mathbf{q} = (\pi/2, \pi/2)$ to $\mathbf{q} = (3\pi/2, 3\pi/2)$ (as is frequently reported in the literature) with the same quantity plotted from $\mathbf{q} = (0,0)$ to $\mathbf{q} = (2\pi, 2\pi)$. The ARPES data employed correspond to an optimally doped Bi2212 sample in the superconducting state[2]. In the restricted momentum view, U_0 yields a spin response with rich momentum structure, resembling the famous "hourglass" shape reported in the literature on other cuprates. However, the wider momentum view reveals two peaks at low energy near $\mathbf{q} = (0,0)$ and $\mathbf{q} = (2\pi, 2\pi)$ three times larger than the rest of the signal (indicated by white arrows in Supplementary Figure 9b). The spin response thus constructed displays an inordinate amount of spectral weight at momenta where experiments do not detect it. This artifact was removed by the choice of coupling function U_q defined in the main text, which suppresses the response around $\mathbf{q} = n(2\pi, 2\pi)$.

We emphasize that such a choice of U_q was not made to favor spin-fluctuation-induced superconductivity models, but was rather motivated by the fact that it rectifies the small-$\mathbf{q}$ intensity problem and yields a spin susceptibility in better agreement with experimental observations. The form of U_q is also supported by Renormalization Group approaches [13] that include the effect of vertex corrections and show a strong enhancement of the spin-susceptibility at (π, π). While the exact form of U_q is indeed not known, the t-J model [14] provides the analytical form which we have used in Eq. (7) in the main text. As was shown in [14], within the t-J model, the constraint of no-double-occupancy simply leads a renormalized band parameters, which are determined from a fit to experimental data.

---

[2]These data were collected from the same sample as those in Supplementary Figure 7, but in the superconducting state.

Validity of the RPA approach

Strictly speaking, RPA-based approaches should be used in weakly correlated systems, which may cast some doubt on the validity of our approach as applied to the cuprates at low doping, where correlations are believed to be strong [15, 16]. However, this notion of extremely strong electronic correlations in the cuprates has recently been challenged by several works [17, 18]. In short, the strength of electronic correlation in cuprates is a debated topic. As to the magnetic excitations in cuprates, there are a large number of RPA-based calculations successfully reproducing experimental observations in the cuprates, even at low doping. For instance, the RPA was successfully employed by Schrieffer et al. in the calculation the exchange energy J and the spin wave spectrum representative of the undoped cuprates, where correlations are believed to be strong [19]. Morr and Pines employed a method which is similar in spirit to the RPA-based calculation in our work, and were able to reproduce the doping dependence of the resonance peak [20]. Their results were similar to those obtained by Brinckmann and Lee [14], who used a slave-boson approach to the t-J model and a RPA with ladder diagram corrections (interestingly, they also found that the renormalization factor coming from these corrections was negligible). Other works in which the RPA has been successfully applied to describe the INS spectra in the cuprates (at different doping levels) can be found in refs. [21–27]. Additionally, earlier work by us [3] and another group [28] shows that the experimentally derived $A(\mathbf{k}, \omega)$ can successfully reproduce the spin-resonance peak and its dispersion in Bi2212 within an RPA-based analysis. Collectively, all these references suggest that RPA-based approaches can successfully describe the cuprate spin response.

Non-resonant excitations in the calculated spin response

Supplementary Figure 10 is the same as Fig. 2d of the main text but in the reduced energy range $[0, 100]$ meV. The white curve is the locus of minima of the quantity $E_k + E_{k+q}$, where q runs along $1/2(\pi, \pi) \rightarrow 3/2(\pi, \pi)$, E_k is the gapped dispersion $E_k = \sqrt{\epsilon_k^2 + \Delta_k^2}$, and Δ_k is the d-wave gap. We have taken $\Delta_0 = 35$ meV as the antinodal gap and a parametrization of the dispersion which gives the Fermi surface in closest agreement with our data for the OP80 sample. This curve marks the threshold of particle-hole excitations allowed in χ_0 by kinematics. The complicated shape of this "particle-hole threshold" is controlled by the d-wave gap and the shape

of the quasiparticle Fermi surface. Non-resonant excitations (due to χ_0 only) are allowed to the right of this line, whereas resonant excitations (due to the RPA denominator) can exist below the p-h continuum. Note the two regions of allowed excitations indicated by the arrows. These regions are located near vectors $q_1 = 0.68(\pi, \pi)$ and $q_2 = 1.33(\pi, \pi)$, which correspond to the two possible node-node scattering vectors in the Fermi surface. The almost linear behavior is a consequence of the steep, almost linear slope of the electronic dispersion in the $\Gamma - Y$ direction. These features lie above the particle-hole continuum, so they are non-resonant and therefore weak. Thus, these features can be understood as non-resonant excitations allowed by the structure of the particle-hole bubble χ_0.

Supplementary Note 5. Alternative estimate of the spin-fermion coupling energy

Mishra et al. [11] pointed out that the the effective electron-electron interaction should be written as

$$V(\mathbf{q}, \Omega) = \frac{3}{2}U^2\frac{\chi_0(\mathbf{q}, \Omega)}{1 - U_q\chi_0(\mathbf{q}, \Omega)}, \tag{4}$$

where the coupling energy U is in general distinct from U_0. This can be best seen when approaching the antiferromagnetic transition at low doping. While the momentum structure of U_q remains largely unchanged, U_0 is renormalized by vertex corrections, in order to satisfy the Adler principle [29]. Following Mishra et al., here we show how U can be obtained from the electron self-energy. In this section, we only report results in the important region near T_c.

Assuming the single-particle renormalizations are due to V, we can estimate the self-energy via

$$\mathrm{Im}\Sigma(\mathbf{k}, \omega) = \frac{1}{N}\sum_{\mathbf{q}}\int \mathrm{d}\Omega[n(\Omega) + f(\Omega - \omega)]\mathrm{Im}V(\mathbf{q}, \Omega)A(\mathbf{k} - \mathbf{q}, \omega - \Omega), \tag{5}$$

where $n(\omega)$ and $f(\omega)$ are the Bose and Fermi distributions, respectively, and the integral is cut off at $\Omega = 0.4$ eV. By Kramers-Kronig relations, we can then obtain the real part of the self-energy and the nodal Fermi velocity renormalization,

$$Z = \frac{v_{\mathrm{F}}^0}{v_{\mathrm{F}}} = 1 - \frac{d}{d\omega}\mathrm{Re}\Sigma(\mathbf{k}_{\mathrm{n}}, \omega)\bigg|_{\omega=0}, \tag{6}$$

where $\mathbf{k}_{\mathrm{n}}$ is the nodal Fermi momentum and v_{F}^0 and v_{F} are the bare and interacting nodal Fermi velocities, respectively. Based on the T-linear behavior of v_{F} inferred from laser ARPES data from optimally doped Bi2212 [30], we estimate that, for the OP80 sample, $Z(70\mathrm{K}) \sim 2.1$ and $Z(90\mathrm{K}) \sim 2$, with similar values for the single crystal OP91. For the UD67 sample we have $Z(62\mathrm{K}) \sim 2.4$ and $Z(80\mathrm{K}) \sim 2.3$ [31]. Using the measured spectral functions and the spin susceptibilities calculated in the main text, we computed Z while adjusting U until we obtained the values above. For all samples, U and U_0 differ by at most 11%, which is somewhat lower than the deviation reported in [11]. Using these coupling energies, the eigenvalues are still essentially equal to unity near T_{c}, as shown in Supplementary Table 1. For comparison, we also included the eigenvalues obtained by assuming $U = U_0$, as in the main text (labeled λ_0).

Supplementary Note 6. Uncertainties in the eigenvalues

The leading eigenvalue in the BSE depends on the spin-fermion coupling through the factor U_0^2 and the denominator of the RPA expression for the spin susceptibility. This coupling, in turn, was fixed from the empirical relation

$$E_{\mathrm{R}} = 5.4 k_{\mathrm{B}} T_{\mathrm{c}}. \tag{7}$$

Therefore, we estimate the uncertainty in the eigenvalue by relaxing the above relation and introducing the uncertainty $\Delta E_{\mathrm{R}} = 10$ meV. This rather large variation was chosen to account not only for the INS energy resolution (< 5 meV), but also for the fact that the energy of the (π, π) peak may vary somewhat with temperature (as

seen, for example, in ref. [32]). Supplementary Figure **11** shows plots of the leading eigenvalue as a function of the coupling U_0 for both thin films above (but close to) T_c. The dashed vertical lines represent the values of U_0 used in the main text and for which the (π, π) peak energy was exactly given by Supplementary Equation 7. The horizontal dashed lines are the resulting eigenvalues (reported in the main text). The horizontal dimension of the shaded rectangles represents the range of U_0 values for which the peak energy moves from $E_R + \Delta E_R$ meV (lowest U_0) to $E_R - \Delta E_R$ meV (highest U_0). The vertical dimension represents the resulting uncertainty in the eigenvalue. Thus, we estimate a $15\% - 20\%$ variation in the leading eigenvalues reported in the main text.

Supplementary References

1. Norman, M. R. Linear response theory and the universal nature of the magnetic excitation spectrum of the cuprates. *Physical Review B* **75,** 184514 (2007).

2. Xu, G. *et al.* Testing the itinerancy of spin dynamics in superconducting $Bi_2Sr_2CaCu_2O_{8+d}$. *Nature Physics* **5,** 642–646 (2009).

3. Chatterjee, U. *et al.* Dynamic spin-response function of the high-temperature $Bi_2Sr_2CaCu_2O_{8+d}$ superconductor from angle-resolved photoemission spectra. *Physical Review B* **75,** 172504 (2007).

4. Randeria, M., Sensarma, R., Trivedi, N. & Zhang, F.-C. Particle-Hole Asymmetry in Doped Mott Insulators: Implications for Tunneling and Photoemission Spectroscopies. *Physical Review Letters* **95,** 137001 (2005).

5. Anderson, P. W. & Ong, N. P. Theory of asymmetric tunneling in the cuprate superconductors. *Journal of Physics and Chemistry of Solids. Spectroscopies in Novel Superconductors 2004* **67,** 1–5 (2006).

6. Feng, D. L. *et al.* Bilayer Splitting in the Electronic Structure of Heavily Overdoped $Bi_2Sr_2CaCu_2O_{8+d}$. *Physical Review Letters* **86,** 5550–5553 (2001).

7. Chuang, Y.-D. *et al.* Bilayer splitting and coherence effects in optimal and underdoped $Bi_2Sr_2CaCu_2O_{8+d}$. *Physical Review B* **69,** 094515 (2004).

8. Dahm, T. *et al.* Strength of the spin-fluctuation-mediated pairing interaction in a high-temperature superconductor. *Nature Physics* **5,** 217–221 (2009).

9. Fetter, A. L. & Walecka, J. D. *Quantum Theory of Many-Particle Systems* (McGraw-Hill, Boston, 1971).

10. Kaminski, A. *et al.* Renormalization of the Spectral Line Shape and Dispersion Below T_c in $Bi_2Sr_2CaCu_2O_{8+d}$. *Physical Review Letters* **86,** 1070–1073 (2001).

11. Mishra, V., Chatterjee, U., Campuzano, J. C. & Norman, M. R. Effect of the pseudogap on the transition temperature in the cuprates and implications for its origin. *Nature Physics* **10,** 357 (2014).

12. Izuyama, T., Kim, D.-J. & Kubo, R. Band Theoretical Interpretation of Neutron Diffraction Phenomena in Ferromagnetic Metals. *Journal of the Physical Society of Japan* **18,** 1025–1042 (1963).

13. Honerkamp, C., Salmhofer, M., Furukawa, N. & Rice, T. M. Breakdown of the Landau-Fermi liquid in two dimensions due to umklapp scattering. *Physical Review B* **63,** 035109 (2001).

14. Brinckmann, J. & Lee, P. A. Slave Boson Approach to Neutron Scattering in $YBa_2Cu_3O_{6+y}$ Superconductors. *Physical Review Letters* **82,** 2915–2918 (1999).

15. Anderson, P. W. *et al.* The physics behind high-temperature superconducting cuprates: the 'plain vanilla' version of RVB. *Journal of Physics: Condensed Matter* **16,** R755 (2004).

16. Gweon, G.-H., Shastry, B. S. & Gu, G. D. Extremely Correlated Fermi-Liquid Description of Normal-State ARPES in Cuprates. *Physical Review Letters* **107,** 056404 (2011).

17. Comanac, A., de'Medici, L., Capone, M. & Millis, A. J. Optical conductivity and the correlation strength of high-temperature copper-oxide superconductors. *Nature Physics* **4,** 287–290 (2008).

18. Jang, S. W. *et al.* Direct theoretical evidence for weaker correlations in electron-doped and Hg-based hole-doped cuprates. *Scientific Reports* **6,** 33397 (2016).

19. Schrieffer, J. R., Wen, X. G. & Zhang, S. C. Dynamic spin fluctuations and the bag mechanism of high-T_c superconductivity. *Physical Review B* **39,** 11663–11679 (1989).

20. Morr, D. K. & Pines, D. The Resonance Peak in Cuprate Superconductors. *Physical Review Letters* **81,** 1086–1089 (1998).

21. Liu, D. Z., Zha, Y. & Levin, K. Theory of Neutron Scattering in the Normal and Superconducting States of $YBa_2Cu_3O_{6+x}$. *Physical Review Letters* **75,** 4130–4133 (1995).

22. Bulut, N. & Scalapino, D. J. Neutron scattering from a collective spin fluctuation mode in a CuO_2 bilayer. *Physical Review B* **53,** 5149–5152 (1996).

23. Norman, M. R. Magnetic collective mode dispersion in high-temperature superconductors. *Physical Review B* **63,** 092509 (2001).

24. Dahm, T., Manske, D. & Tewordt, L. Collective modes in high-temperature superconductors. *Physical Review B* **58,** 12454–12458 (1998).

25. Norman, M. R. Relation of neutron incommensurability to electronic structure in high-temperature superconductors. *Physical Review B* **61,** 14751–14758 (2000).

26. Kao, Y.-J., Si, Q. & Levin, K. Frequency evolution of neutron peaks below T_c: Commensurate and incommensurate structure in $La_{0.85}Sr_{0.15}CuO_4$ and $YBa_2Cu_3O_{6.6}$. *Physical Review B* **61,** R11898–R11901 (2000).

27. Onufrieva, F. & Pfeuty, P. Spin dynamics of a two-dimensional metal in a superconducting state: Application to the high-T_c cuprates. *Physical Review B* **65,** 054515 (2002).

28. Inosov, D. S. *et al.* Relation between the one-particle spectral function and dynamic spin susceptibility of superconducting $Bi_2Sr_2CaCu_2O_{8-d}$. *Physical Review B* **75,** 172505 (2007).

29. Chubukov, A. V., Monthoux, P. & Morr, D. K. Vertex corrections in antiferromagnetic spin-fluctuation theories. *Physical Review B* **56,** 7789–7792 (1997).

30. Plumb, N. C. *et al.* Low-Energy (< 10 meV) Feature in the Nodal Electron Self-Energy and Strong Temperature Dependence of the Fermi Velocity in $Bi_2Sr_2CaCu_2O_{8+d}$. *Physical Review Letters* **105,** 046402 (2010).

31. Vishik, I. M. *et al.* Doping-Dependent Nodal Fermi Velocity of the High-Temperature Superconductor $Bi_2Sr_2CaCu_2O_{8+d}$ Revealed Using High-Resolution Angle-Resolved Photoemission Spectroscopy. *Physical Review Letters* **104,** 207002 (2010).

32. Dai, P. *et al.* The Magnetic Excitation Spectrum and Thermodynamics of High-T_c Superconductors. *Science* **284,** 1344–1347 (1999).